BIOCHEMISTRY

A quantitative biology approach correlates neuronal toxicity with the largest inclusions of TDP-43

Roberta Cascella[1]†, Alessandra Bigi[1]†, Dylan Giorgino Riffert[1], Maria Cristina Gagliani[2], Emilio Ermini[1], Matteo Moretti[1], Katia Cortese[2], Cristina Cecchi[1]*, Fabrizio Chiti[1]*

A number of neurodegenerative conditions are associated with the formation of cytosolic inclusions of TDP-43 within neurons. We expressed full-length TDP-43 in a motoneuron/neuroblastoma hybrid cell line (NSC-34) and exploited the high-resolution power of stimulated emission depletion microscopy to monitor the changes of nuclear and cytoplasmic TDP-43 levels and the formation of various size classes of cytoplasmic TDP-43 aggregates with time. Concomitantly, we monitored oxidative stress and mitochondrial impairment using the MitoSOX and MTT reduction assays, respectively. Using a quantitative biology approach, we attributed neuronal dysfunction associated with cytoplasmic deposition component to the formation of the largest inclusions, independently of stress granules. This is in contrast to other neurodegenerative diseases where toxicity is attributed to small oligomers. Using specific inhibitors, markers, and electron microscopy, the proteasome and autophagy were found to target mainly the largest deleterious inclusions, but their efficiency soon decreases without full recovery of neuronal viability.

INTRODUCTION

A number of neurodegenerative conditions are associated with a common histopathology within neurons of the central nervous system, consisting in the formation of cytosolic inclusion bodies of TAR DNA-binding protein 43 (TDP-43) in these cells (1–4). This process is associated with the mislocalization of the protein from the nucleus, where it normally resides and plays its function, to the cytosol, where it forms well-defined skein-like or round inclusions, where TDP-43 is, in part, proteolyzed, hyperphosphorylated, and polyubiquitinated (1–3, 5, 6). It is increasingly recognized that TDP-43 proteinopathies originate from a combination of a loss-of-function (LOF) mechanism, resulting from TDP-43 depletion in the nucleus, and a gain-of-function (GOF) mechanism, resulting from TDP-43 accumulation in the cytosol (7, 8).

This common histopathology is found in all cases of sporadic amyotrophic lateral sclerosis (sALS) and in most patients suffering from familial forms of the disease (fALS), with the exception of cases associated with mutations of superoxide dismutase-1 (SOD1), RNA-binding protein fused in sarcoma (FUS), and, frequently, chromosome 9 open reading frame 72 (C9orf72) (3). In sALS and fALS, TDP-43 inclusions accumulate in the motor neurons of the primary motor cortex, corticospinal tracts, brainstem and spinal cord, and glial cells, as well as in the neurons of the hippocampus and frontotemporal cortex in a subset of patients (1, 2, 4). TDP-43 pathology is also observed in frontotemporal lobar degeneration with ubiquitin-positive inclusions (FTLD-U or FTLD-TDP), where the intraneuronal deposits are mainly present in the frontal and temporal cortices and in the hippocampus and their glial cells (1, 2). Moreover, TDP-43 inclusions are frequently found in the brain of patients with Alzheimer's disease (AD) (9), Parkinson's disease (PD) (10), Huntington's disease (11), and other neurodegenerative conditions (12), emphasizing its high propensity to aggregate in a wide spectrum of neurologically compromised situations.

The conversion of cytoplasmic TDP-43 from its soluble form into mature inclusions appears to be a complex and not yet understood process. Under conventional immunohistochemistry, the inclusions appear either skein-like or compact and rounded (1–4, 13). Round inclusions range from 1 to 25 μm in diameter in neurons, although smaller species are likely to be present and escape detection because of microscopical resolution limitation (3, 4, 13, 14). Skein-like species are ca. 0.5 to 1.0 μm in diameter and up to 15 μm in length (3, 4, 13, 14). Histopathologists have repeatedly reported transmission electron microscopy (TEM) images of 10- to 20-nm-wide filaments containing TDP-43 within neurons or motor neurons of patients with ALS and FTLD (5, 9, 15, 16), in the absence of Congo red or thioflavin S binding (17–20). A recent study by cryo–electron microscopy has revealed the molecular structure of the protease-resistant portion of filaments extracted from the cortex of two cases with a history of ALS associated with FTLD-U (21). In this structure, residues 282 to 360 from TDP-43 molecules stack on each other in a parallel, in-register fashion at 4.8 Å distance and 1.4° angles to form a right-handed double-spiral fold (21). Each TDP-43 molecule forms 10 very short β strands alternated by large stretched of turns, and the β sheets do not stack on each other and do not form, consequently, the cross-β structure typical of amyloid fibrils. The smooth protofilament surface also appears devoid of the deep and nonpolar grooves required to bind amyloid-diagnostic dyes (21). One of the complexities of TDP-43 inclusion formation lies in the ability of the protein to undergo liquid-liquid phase separation not only in vitro (20, 22, 23) but also in vivo within stress granules (SGs) or other nuclear or cytoplasmic liquid droplets (24–26).

Despite this acquired knowledge on TDP-43 inclusions, the mechanism through which the inclusions form remains elusive. Moreover, it is not clear how the inclusions contribute to neuronal dysfunction and the identity of the most deleterious species among those that differ in morphology, size, phase, and clearance status. In this work, we have expressed human full-length TDP-43 in a motor neuron/neuroblastoma hybrid cell line and in a more classical neuroblastoma cell line and have exploited the high resolution of stimulated emission depletion (STED) microscopy to monitor the formation of various classes of cytoplasmic TDP-43

[1]Department of Experimental and Clinical Biomedical Sciences "Mario Serio", University of Florence, 50134 Florence, Italy. [2]Department of Experimental Medicine, Cellular Electron Microscopy Laboratory, University of Genova, 16132 Genova, Italy.
*Corresponding author. Email: cristina.cecchi@unifi.it (C.C.); fabrizio.chiti@unifi.it (F.C.)
†These authors contributed equally to this work.

aggregates as a function of time. We have used an approach of quantitative biology to analyze simultaneously the time courses of TDP-43 nuclear levels, TDP-43 cytoplasmic levels, formation of cytoplasmic aggregates of various sizes, and neuronal dysfunction to develop a model of TDP-43 inclusion body formation and follow closely the link between neuronal dysfunction and specific aggregate types. We will show that neuronal dysfunction is associated with both nuclear depletion and cytoplasmic accumulation of TDP-43 and that the neuronal dysfunction component associated with cytoplasmic deposition arises from the largest inclusions rather than the small ones, unlike observations in other neurodegenerative diseases and the common assumption that the most deleterious species in protein misfolded diseases are the smallest protein oligomers. We will also show that the proteasome and autophagy target particularly these largest inclusions, but their efficiency is compromised in the presence of these species without full recovery of neuronal viability.

RESULTS

Both nuclear depletion and cytoplasmic accumulation of TDP-43 are relevant for neuronal dysfunction

Redistribution of TDP-43 from the nucleus to the cytoplasm is commonly observed when expressing C-terminal fragments (27–29) or mutants of the nuclear localization signal (30–32) in cultured cells, but it also has been observed in our laboratory using high doses of the pCI-neo plasmid expressing the full-length wild-type protein (8). Most of the studies reported in the literature have showed a nuclear enrichment of TDP-43 in the absence of cytosolic mislocalization, following overexpression of full-length TDP-43 in cell cultures (27–31). However, unlike other studies, we have used in our transfection procedure the pCI-neo plasmid, a high plasmid quantity (20 μg), a well-defined cell density, and an advanced lipid nanoparticle technology with superior transfection efficiency (see Materials and Methods for details) (8).

We therefore carried out the present study by transiently transfecting a pCI-neo plasmid (20 μg) expressing human full-length TDP-43 in NSC-34 cells, which is a motor neuron/neuroblastoma hybrid cell line that expresses several motor neuron features (33), and by monitoring the cells over time using STED super-resolution microscopy and polyclonal anti–TDP-43 antibodies that recognize both endogenous (murine) and exogenously expressed (human) TDP-43. Using the same cellular and expression system, cytoplasmic TDP-43 was found in a previous report to be phosphorylated, ubiquitinated, and partially proteolyzed (8), thus recapitulating the biochemical and histopathological features observed in vivo under pathological conditions (1–3).

Transfected cells showed a progressive increase of nuclear TDP-43–derived fluorescence up to ca. 24 hours after transfection, followed by a progressive reduction with a minimum reached at ca. 48 hours, and then a new increase up to nearly physiological values at 72 hours (Fig. 1, A and B). Concomitantly, a progressive accumulation of TDP-43 was observed in the cytoplasm, with a maximum at 40 hours, followed by a gradual decrease (Fig. 1, A and B). In particular, we observed the formation of inclusions with both round and filamentous morphology at 40 hours (Fig. 1A, zoom), which are better visualized in a three-dimensional (3D) reconstruction of the whole cell using wheat germ agglutinin (WGA) to label the membrane (red) and monoclonal anti-human TDP-43 antibodies (green) that recognized

only the exogenously expressed protein (Fig. 1C). The TDP-43 inclusions accumulating in the cytoplasm over time appeared to be phosphorylated at S409/410, with a maximum at 40 hours after cell transfection, as shown by STED microscopy using anti–phospho–TDP-43 (pS409/410) antibodies (fig. S1).

We then monitored the time course of cell viability in the same cellular system and conditions, using two distinct readouts, such as the 3-4,5-dimethylthiazol-2,5-diphenyltetrazolium bromide (MTT) reduction and the MitoSOX assays, which report on the ability of cell mitochondria to reduce MTT and on the levels of mitochondrial superoxide ions, respectively. Cells decreased and then increased their viability, with well-defined kinetics that appeared to be very similar with the two probes [Fig. 2, A and B (black lines), and fig. S2]. These characteristic time courses were analyzed quantitatively with a model that attributes the decreases of cell viability to both depletion of nuclear TDP-43 and accumulation of cytoplasmic protein (see Materials and Methods for details). With the terms "nuclear depletion" and "cytoplasmic accumulation," we do not imply a simple transfer of nuclear TDP-43 to the cytoplasm, as expression and degradation of TDP-43 are also ongoing. We rather intend observable decrease and increase of nuclear and cytoplasmic TDP-43 levels, respectively. In our cell model, MTT reduction at a given time point t [MTT-R(t)] was redetermined theoretically using Eq. 1, which provides MTT-R(t) from the corresponding experimental changes of cytoplasmic and nuclear and TDP-43 at the same time t relative to time 0 hours [$\Delta C(t)$ and $\Delta N(t)$, respectively], weighted for their specific proportionality constants c and n, which were kept constant at all time points (Fig. 2A, gray line). The same analysis was carried out for the values of mitochondrial superoxide ion production [MitoSOX(t)] using Eq. 2 (Fig. 2B, gray line). In both cases, the theoretical model reproduces the experimental time course of cell viability with satisfactory accuracy ($R > 0.95$, $P < 0.001$ in both cases). When the analysis was repeated by considering only nuclear depletion or only cytoplasmic accumulation as sources of toxicity [Fig. 2, C and D (gray dashed and dotted lines, respectively)], the agreement between theoretical and experimental MTT-R(t) or MitoSOX(t) values was not satisfactory.

We then used the determined proportionality constants n and c to quantify the weights of nuclear depletion and cytoplasmic accumulation in determining MTT-R(t) and MitoSOX(t), as detailed in Materials and Methods. The two relative contributions were estimated as 59 ± 3% and 41 ± 3% using the MTT-R(t) analysis, respectively, and 57 ± 3% and 43 ± 3% using the MitoSOX(t) values, respectively, indicating that both nuclear depletion and cytoplasmic accumulation are relevant in determining TDP-43–related toxicity in this cellular system.

To extend the analysis to a different cell type, we acquired time courses of TDP-43 levels and MTT reduction on human neuroblastoma SH-SY5Y cells under identical conditions of transfection (fig. S3). We found similar time courses for the levels of nuclear and cytoplasmic TDP-43 relative to NSC-34 cells, with the former increasing up to 24 hours, then decreasing up to 40 hours, and then increasing again slowly with time and the latter accumulating 40 to 48 hours after cell transfection (fig. S3, A and B). The two phases before and after 40 hours correspond to a decrease and then increase of cell viability, respectively, as assessed with the MTT reduction assay (fig. S3C). The results were similar to those obtained with NSC-34 cells under corresponding conditions, confirming the overall mechanism in an independent cell line.
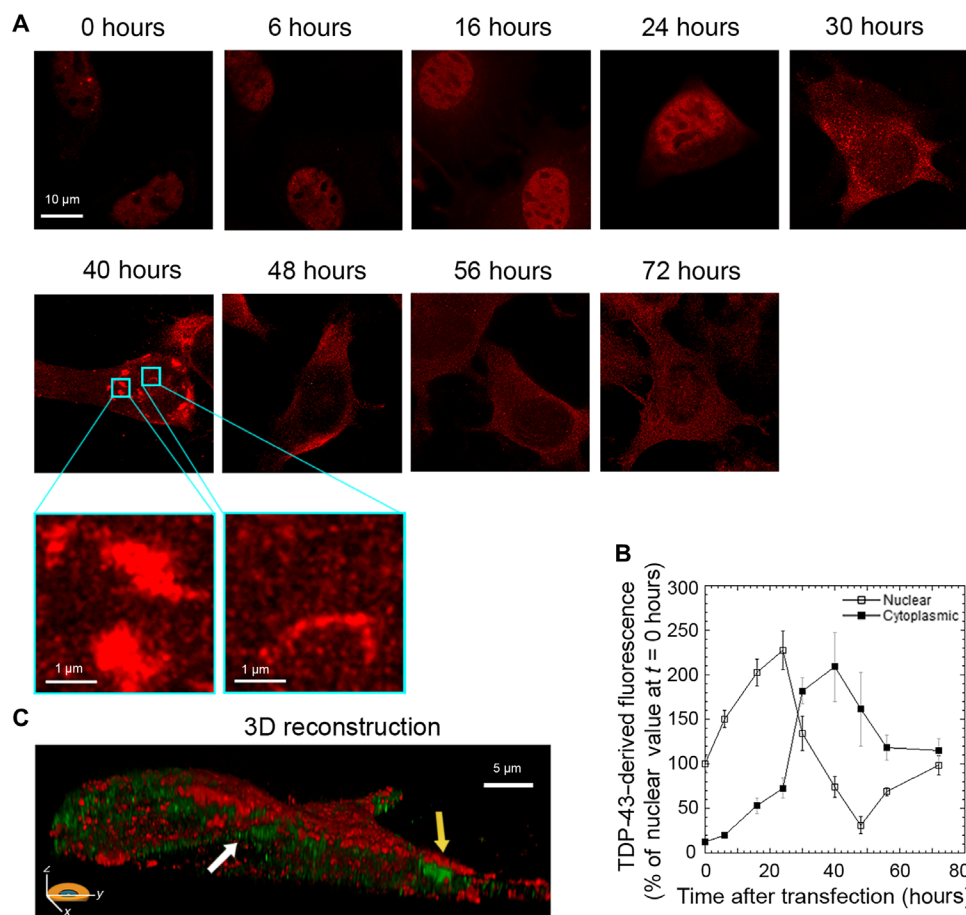
Fig. 1. Overexpression of TDP-43 caused a redistribution of TDP-43 between the nucleus and the cytoplasm. (**A**) Representative STED microscopy images of NSC-34 cells ($n = 3$) transfected with 20 μg of pCI-neo plasmid expressing human TDP-43 and analyzed at different lengths of time after transfection. Red fluorescence, total TDP-43 (endogenous and exogenous). Higher magnifications show round (left) and filamentous (right) TDP-43 inclusions. (**B**) Time courses of nuclear and cytoplasmic TDP-43–derived fluorescence determined over 200 to 250 NSC-34 cells and expressed as a percentage of the value for cells transfected for 0 hours, taken as 100% ($n = 3$). (**C**) 3D reconstruction of the z-stack analysis (5-μm-thick slices) of the specimens shown in (A) (40 hours). Red and green fluorescence, cell membrane (WGA) and exogenous (human) TDP-43, respectively. An NSC-34 cell was virtually dissected on the zy plane to show more clearly the intracellular TDP-43 inclusions. Yellow and white arrows, round and filamentous inclusions, respectively.

Time courses of different size classes of TDP-43 inclusions

We used the high resolution of STED microscopy to discriminate between different size classes of cytoplasmic TDP-43 inclusions, which were identified, sorted on the basis of their size, and counted one by one in each analyzed cell, as described in Materials and Methods and exemplified in Fig. 3A and fig. S4. We chose seven classes of aggregates with increasing diameter (0.025 to 0.15 μm, 0.15 to 0.25 μm, 0.25 to 0.50 μm, 0.50 to 0.75 μm, 0.75 to 1.00 μm, 1.00 to 1.50 μm, and >1.50 μm). We excluded class 7 (>1.50 μm) because the inclusions were too scarce to carry out a statistically meaningful analysis. The number of each inclusion size class (n) divided by the cytoplasmic area of the neurons (A, units of μm^2) yielded its density (D, units of n/μm^2). For each inclusion size class, D multiplied by its mean area yielded the density of fluorescence associated with that given inclusion class [$F(t)/A$]. Individual large inclusions appeared homogenous in fluorescence distribution, without small areas devoid of fluorescence inside, ruling out that they resulted from a number of smaller noninteracting inclusions populating a small area with high density and imaged as single large inclusions. This approach allows the distinction of inclusions in different size classes

but do not intend to determine their precise sizes due to the steric hindrance of the antibodies used to image them.

Figure 3B shows the time courses of fluorescence density [$F(t)/A$] associated with each of the six size classes of cytoplasmic inclusions, whereas Fig. 3C shows the time courses of total fluorescence [again, $F(t)/A$] for the six aggregate types together. The kinetics are very different for the six inclusion classes. Smaller inclusions (diameter, 0.025 to 0.15 μm) appear to form first and then decay more slowly as they convert into larger aggregates, whereas larger aggregates form later, on a time scale similar to that by which smaller aggregates decay and with a delay increasing with inclusion size. The three largest inclusions appear to decay at later times, whereas the two smaller species increase concomitantly in population.

Identification of the mechanism of TDP-43 inclusion formation and toxic inclusions by a quantitative analytical approach

We analyzed the various kinetic traces with a number of theoretical models. The only model that could describe all time courses simultaneously was based on three exponential phases, all preceded by
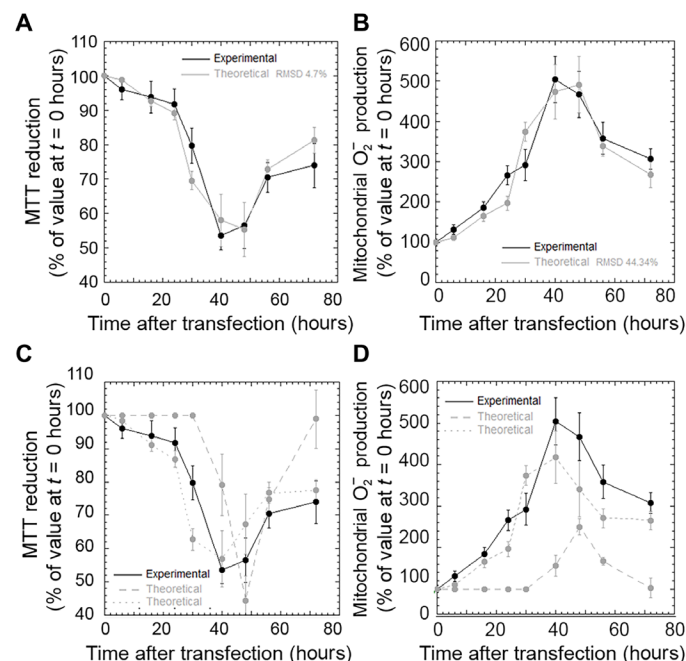
Fig. 2. Both nuclear depletion and cytoplasmic accumulation of TDP-43 are relevant for neuronal dysfunction. (**A** to **D**) Experimental (black) and theoretical (gray) time courses of MTT reduction (A and C) ($n = 3$) and mitochondrial superoxide production (B and D) ($n = 3$) in NSC-34 cells treated as in (A). The theoretical traces refer to nuclear depletion and cytoplasmic accumulation together (gray solid lines), only nuclear depletion (gray dashed lines), and only cytoplasmic accumulation (gray dotted lines). Experimental errors are SEMs. The degree of agreement [root mean square deviation (RMSD)] between experimental and theoretical analyses is also reported.

a lag time, where the first phase consisted in the formation of the smaller inclusions (0.025 to 0.15 μm), the second in the conversion of each size class into the larger one, and the third into a clearance or disassembly process that converted the larger species into smaller ones (see Materials and Methods for an analytical description). In particular, all six time courses were described by a complex three-phase sigmoid function of logistic type (Eq. 4 or 5), resulting from a simultaneous multiple-fitting procedure, where the same values of rate constants (1, 0.2, and 0.4 hour^{-1} for the k_1, k_2, and k_3 rate constants, respectively) and lag times (12 and 58 hours for the first/second and third phases, respectively, delayed by a constant value of 6 hours and anticipated by a constant value of 2 hours for each step of inclusion size increase, respectively) could describe satisfactorily all the kinetic traces simultaneously. The agreement between experimental and theoretical time courses is shown in Fig. 3C and Fig. 3 (D to I), for all the inclusions together and for the individual inclusion classes, respectively ($R > 0.95$, $P < 0.001$ for all size classes). The complete analytical kinetic traces are shown in fig. S5.

After the identification of the three phases in the various time courses and of the variability observed among the kinetic traces, the question naturally arises as to their meaning in terms of a mechanistic description of TDP-43 inclusion formation in the cytoplasm. The smallest aggregates (diameter, 0.025 to 0.15 μm) appear to form very rapidly, through an exponential phase that is not apparent for the other size classes (Fig. 3, B and D). This phase may represent aggregation of initially native TDP-43 transferred to the cytoplasm or translocation of small liquid assemblies from the nucleus. The
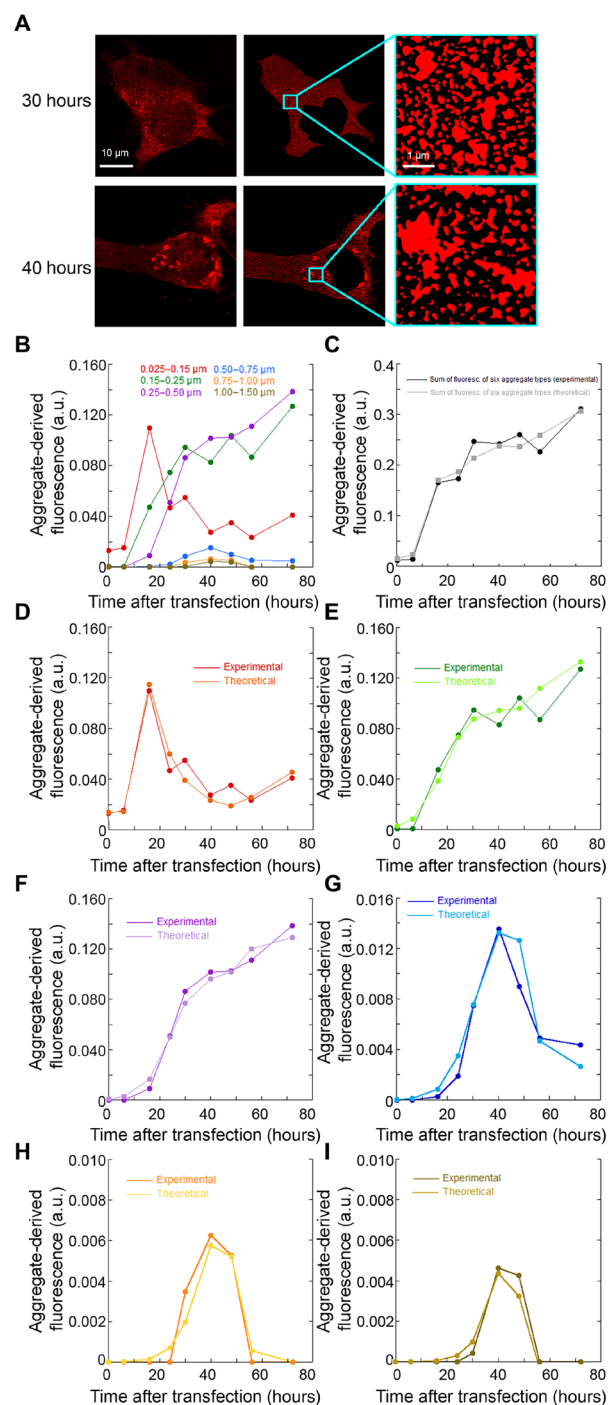

Fig. 3. Time courses of different size classes of TDP-43 inclusions. (**A**) Approach used to identify size classes of TDP-43 inclusions: STED microscopy images of NSC-34 cells ($n = 3$) transfected with pCI-neo plasmid expressing human TDP-43 (left) were treated to exclude the nucleus area, after background subtraction, to obtain a better definition of the cytoplasmic inclusions (middle) and magnified to identify inclusions (right) and count them, as described in Materials and Methods. (**B**) Time courses of fluorescence density [$F(t)/A$] associated with each of the six size classes of cytoplasmic TDP-43 inclusions. (**C**) Experimental and theoretical time courses of total fluorescence density [$F(t)/A$] for the six aggregate types together. (**D** to **I**) Experimental and theoretical time courses of fluorescence density [$F(t)/A$] for the individual inclusion classes: diameters of 0.025 to 0.15 μm (D), 0.15 to 0.25 μm (E), 0.25 to 0.50 μm (F), 0.50 to 0.75 μm (G), 0.75 to 1.00 μm (H), and 1.00 to 1.50 μm (I). a.u., arbitrary units.

inclusions belonging to bigger classes form later, with a clear lag time whose length increases with inclusion size but with a new slower exponential phase whose rate constants are similar in the various cases and similar to that of the small aggregate decay (Fig. 3, B and E to I). This indicates that large inclusions (diameter, >0.15 μm) originate from the growth or conversion of the first species (0.025 to 0.15 μm) into progressively bigger inclusions in a continuum of size increase, whereas the smallest species (0.025 to 0.15 μm) form readily, through an independent and more rapid process. The three biggest inclusions (diameter, >0.50 μm) then decay into species with intermediate size (0.15 to 0.50 μm) through a process of clearance or disassembly that will be considered below.

Another important question that arises is whether the observed time courses of toxicity detected with the MTT reduction and MitoSOX assays can be assigned to well-defined inclusion sizes. The theoretical approach that we have used allows us to dissect the reconstructed time course of toxicity into its two individual components arising from the redistribution of TDP-43 between the nucleus and the cytoplasm (Fig. 4A). The component of toxicity associated with cytoplasmic accumulation (Fig. 4A, dotted line) has a time course that overlaps with that of the largest species having a diameter >0.50 μm [Fig. 4, B and C (blue/orange/brown traces)], indicating that the toxicity attributable to cytoplasmic TDP-43 accumulation is mainly associated with the presence of the largest inclusions. Moreover, using the two classes of 0.025 to 0.15 μm and 0.5 to 0.75 μm that have a fluorescence-derived value of the same order of magnitude at critical time points and are therefore comparable, we see a correlation between MTT reduction derived from the cytoplasmic component and inclusion population only for the latter largest class (Fig. 4D).

GU-rich RNA prevents TDP-43 mislocalization and aggregation

To assess, in our cellular and expression system, the effect of an RNA molecule acting as a good TDP-43 binder, we monitored nuclear and cytoplasmic TDP-43 levels following the addition of a 12-nucleotide GU-rich RNA molecule, which has been reported to maintain TDP-43 in soluble form or reduce the amount of the aggregates (*34*). The NSC-34 cells were transfected with 20 μg of pCI-neo plasmid expressing human TDP-43 in the absence or presence of the GU-rich RNA, at a concentration of 1 or 10 μM, either cotransfected with the pCI-neo plasmid or transfected 24 hours later. STED microscopy images acquired at 40 hours after plasmid transfection showed that the RNA prevented the mislocalization of TDP-43 in the cytoplasm, maintaining the protein in the nucleus (fig. S6A). Concomitantly, RNA treatment also appeared to prevent cell dysfunction, as assessed by the MTT reduction assay, independently of the time of RNA transfection (fig. S6B).

Large inclusions are degraded by proteasome and autophagy

At later times, all large inclusions (diameter, >0.50 μm) decay over time, and intermediate-size species (0.15 to 0.50 μm) increase concomitantly in population, through a third exponential phase with apparently similar rate constants in the two cases (Fig. 3). To understand whether the autophagy-lysosomal pathway (ALP) and the ubiquitin-proteasome system (UPS) were activated and responsible for this process, cells were treated with either the UPS inhibitor MG132 or the ALP inhibitor 3-methyladenine (3-MA) at 38 hours after transfection. Large inclusions appear to remain in the cytoplasm
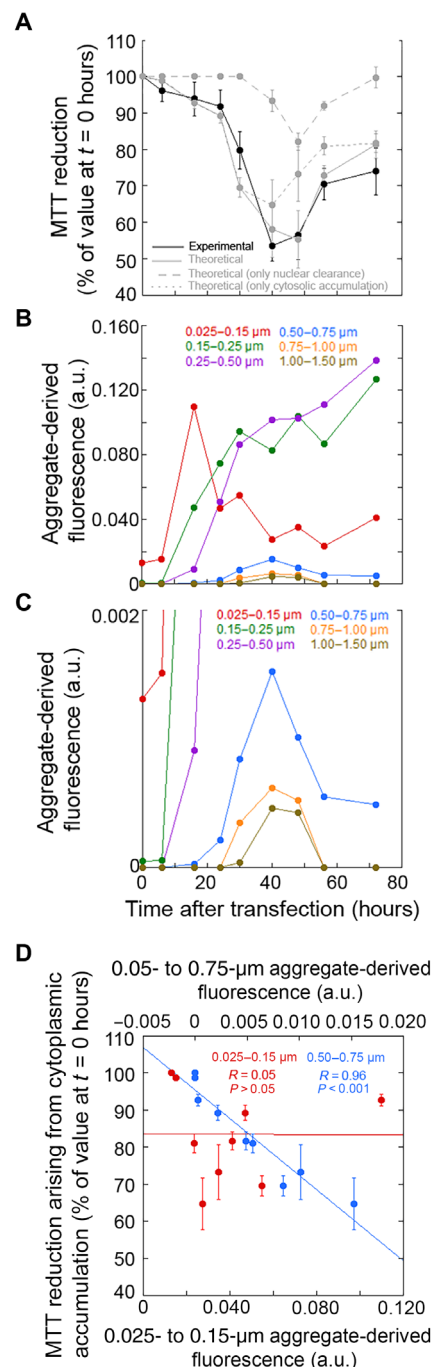

Fig. 4. Identification of the mechanism of TDP-43 inclusion formation and toxic inclusions by a quantitative analytical approach. (**A**) Experimental (black line) and theoretical (gray solid line) time course analysis of MTT reduction (*n* = 3), expressed as the percentage of the value for cells transfected at 0 hours (taken as 100%). The theoretical contributions of nuclear depletion (dashed line) and cytoplasmic accumulation (dotted line) are also shown. Experimental errors are SEMs. (**B** and **C**) Experimental time courses for the individual inclusion classes (same as those in Fig. 3B). Classes 4 to 6 are magnified in the second panel. (**D**) Dependence of the contribution of TDP-43 cytoplasmic accumulation to MTT reduction on the aggregate-derived fluorescence of the indicated size classes. Experimental errors are SEMs.

at 56 and 72 hours after transfection, suggesting that both UPS and ALP contribute to the clearance of large aggregated TDP-43 (Fig. 5A). In both cases, however, the number of inclusions at 72 hours decreases, relative to 40 hours, upon inhibitor treatment, indicating that inhibition of only one system maintains the inclusion clearance through the noninhibited system (Fig. 5A). We also

found that 40 hours after cell transfection, cytoplasmic TDP-43 inclusions strongly colocalized with both lysosomes and early endosomes (Fig. 5, B and C), confirming the involvement of ALP in the clearance of TDP-43 inclusions.

TEM images show a few small electron-dense inclusions in vehicle-transfected cells and immediately after the 3-hour window of transfection
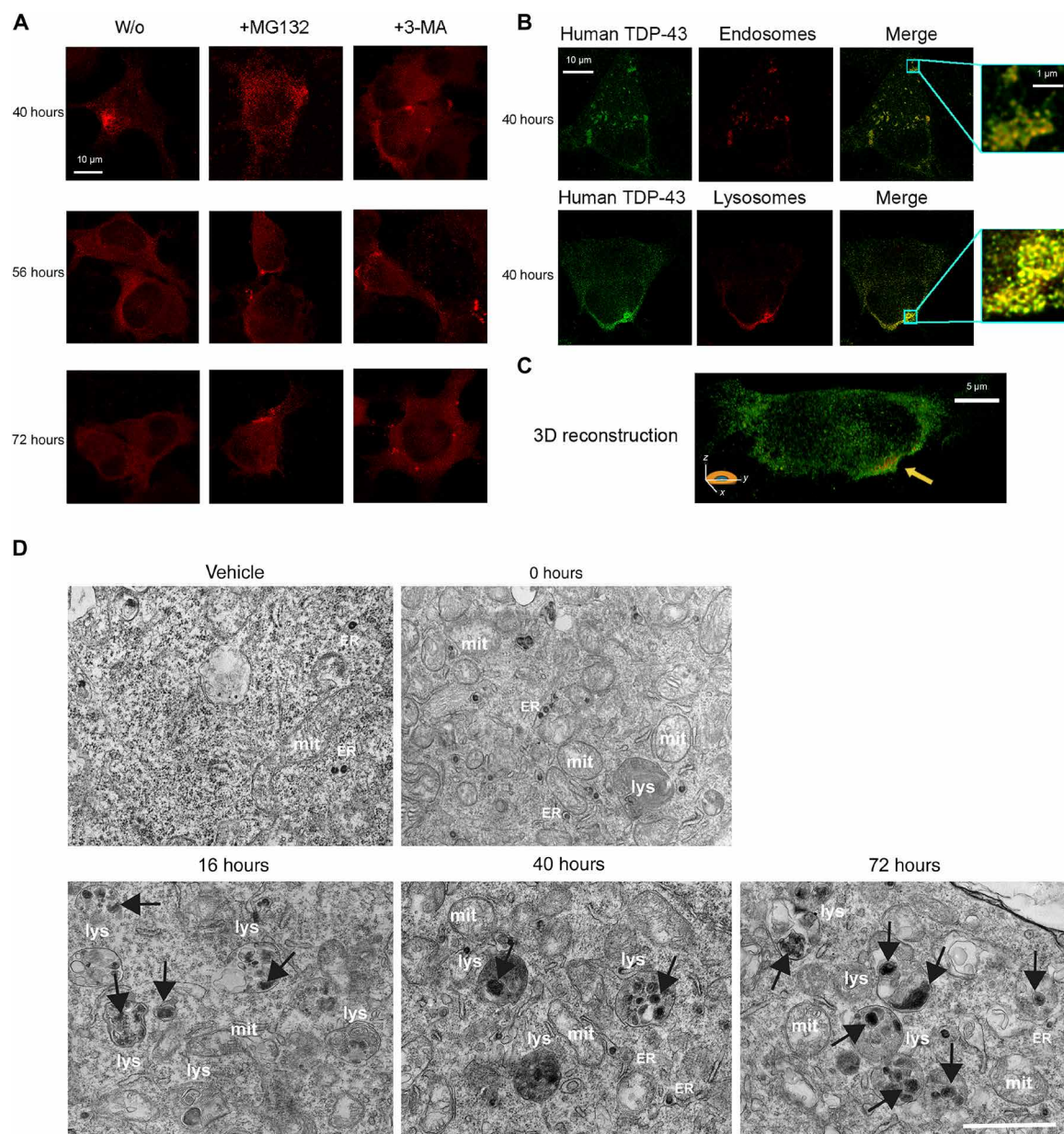

Fig. 5. Large inclusions are degraded by proteasome and autophagy. (**A**) Representative STED microscopy images of NSC-34 cells ($n = 3$) with 20 μg of pCI-neo plasmid expressing human TDP-43, treated at 38 hours following cell transfection with 5 μM MG132 or 10 mM 3-MA and analyzed 40, 56, and 72 hours after transfection. Red fluorescence, total TDP-43 (human and murine). (**B**) Representative STED microscopy images of NSC-34 cells ($n = 3$) transfected with 20 μg of pCI-neo plasmid expressing human TDP-43 and analyzed 40 hours after transfection. Green and red fluorescence, human TDP-43 (exogenous) and endosomes (top) or lysosomes (bottom), respectively. Magnification boxes, areas with TDP-43 assemblies with a high degree of colocalization with endosomes (top) or lysosomes (bottom). (**C**) 3D reconstruction of the z-stack analysis (5-μm-thick slices) of the specimens shown in (B), bottom right. An NSC-34 cell was virtually dissected on the zy plane to show more clearly the intracellular TDP-43 inclusions colocalizing with lysosomes. (**D**). Representative TEM images of NSC-34 cells ($n = 3$) transfected with vehicle or 20 μg of pCI-neo plasmid expressing TDP-43 and analyzed 0, 16, 40, and 72 hours after transfection. Labels indicate lysosomes (lys), mitochondria (mit), and rough endoplasmic reticulum (ER). Black arrows, cytoplasmic TDP-43 inclusions. Scale bar, 1 μm.

with plasmid expressing TDP-43 (0 hours), often localized within the endoplasmic reticulum (Fig. 5D). These species were previously observed in nontransfected NSC-34 cells (35, 36) and therefore appear to be independent of TDP-43 transfection. At 16 hours, we observed an increase in number of bona fide lysosomes, single-membrane spherical structures with diameters between 200 nm and >1 μm filled with electron-dense materials, featuring large numbers of electron-dense inclusions with a diameter lower than 0.15 μm (Fig. 5D, black arrows), in agreement with the STED analysis (Fig. 3B). Lysosomes increased in number at 40 hours, in which the inclusions are bigger, in the range of 0.50 to 1.50 μm (Fig. 5D, black arrows). In agreement with the STED analysis (Fig. 3B), 40 hours represent the only time when cytoplasmic TDP-43 localized in large vesicles (ca. 1 μm) labeled with lysosomal markers (Fig. 5, B and C). At 72 hours, the largest inclusions are no longer visible, and most of them are in the range of 0.025 to 0.50 μm (Fig. 5D, black arrows), again, in accordance with STED microscopy (Fig. 3B). The inclusions appear in most cases localized within the lysosomal compartment, suggesting that they are handled by the ALP (Fig. 5D).

TDP-43 is recruited to SGs, but the formation of TDP-43 inclusions is driven by different pathways

We monitored the colocalization of TDP-43 inclusions with four different markers of SGs, such as ataxin-2 (37), T cell intracellular antigen 1 (TIA-1) and TIA-1–related protein (TIAR) (38), eukaryotic initiation factor 3η (eIF3η) (39), and fragile X mental retardation 1 (FMR1) (40). Forty hours after cell transfection, TDP-43 assemblies colocalized with Ataxin-2, TIA-1/TIAR, and eIF3η, as well as with FMR1, albeit to a lesser extent (Fig. 6A, bottom box magnifications). Nevertheless, some TDP-43 aggregates showed only a minor or no colocalization with SGs (Fig. 6A, top box magnifications). A 3D reconstruction of a whole cell also shows the presence of cytoplasmic TDP-43 inclusions with or without colocalization with Ataxin-2 as a representative SG marker (Fig. 6B). Arsenite treatment (0.5 mM, 1 hour) in nontransfected cells, used here as a positive control of SG formation, caused endogenous TDP-43 to accumulate in amorphous cytosolic inclusions colocalizing more extensively with the four SG markers (fig. S7).

The smallest TDP-43 inclusions accumulating at 16 hours (diameter, 0.025 to 0.15 μm) did not exhibit any detectable sign of colocalization with ataxin-2, chosen as a representative SG marker, indicating that they do not consist of small TDP-43 oligomers within SGs (Fig. 6C). A progressive, yet partial, colocalization of TDP-43 assemblies with Ataxin-2 was observed (Fig. 6C, yellow arrows), which reached the maximum value at 40 hours after cell transfection, when the highest cytotoxicity was also observed. The two processes with and without colocalization with the SG marker were apparently concomitant on the time scale and were not sequential, indicating that SG-independent inclusions did not arise from SG-colocalized assemblies or vice versa. Large inclusions were then found to convert into small ones at 56 and 72 hours, for both ataxin-2–positive and ataxin-2–negative assemblies (Fig. 6C).

The TDP-43 inclusions at 40 hours were also studied using fluorescence recovery after photobleaching (FRAP), which allows us to determine whether they adopt a liquid, gel-like, or solid phase (24, 41). For this experiment, NSC-34 cells were transfected with a plasmid coding for human TDP-43 C-terminally fused to the fluorescent tdTOMATO protein. Half of the studied inclusions did not show any FRAP, indicating that they were solid, whereas half of

them showed partial FRAP (Fig. 6D). In particular, in the latter species, the recovery was ca. 10 to 15% and occurred with a $t_{1/2}$ of 5 to 10 s, thus to an extent and on a time scale normally observed for aged SGs that are in a gel-like state transiting into a solid phase (24, 41).

DISCUSSION

Our quantitative model not only allows TDP-43–induced neuronal dysfunction to be dissected into its individual contributions associated with decrease and increase of TDP-43 levels in the nucleus and cytoplasm, amounting to ca. 55 to 60% and 40 to 45%, respectively, in agreement with quantifications obtained previously with a very different approach (8), but also allows us to reveal the relative time courses of the two contributions (Fig. 4). The time course of neuronal toxicity arising from cytoplasmic accumulation was found to overlap with that associated with the formation and disappearance of the largest aggregates rather than the smallest or intermediate ones.

This finding is not obvious in neurodegenerative diseases, where cell toxicity is often associated with small protein oligomers, such as in AD, PD, and Creutzfeldt-Jakob disease (42–45). However, TDP-43 proteinopathies such as ALS and FTLD-TDP are different. Histopathological investigation of postmortem biopsies of spinal cords, hippocampus, or cortex has revealed the presence of large round (up to 25 μm in diameter) or filamentous (0.5 to 1.0 μm in diameter and up to 15 μm in length) inclusions that appear to be even larger than those imaged here (3, 4, 13, 14). More importantly, neuronal loss has been found to correlate with the number of cytoplasmic inclusions in the spinal cord motor neurons and glial cells in distinct groups of patients with ALS (4, 13, 46, 47). Such a correlation between neuronal loss and number of large TDP-43 inclusions, detectable with conventional microscopy and analyzable only postmortem, is also found here in real time in a cellular model where TDP-43 inclusion formation and disappearance are monitored in parallel with neuronal dysfunction arising solely from TDP-43 mislocalization. The results provide a molecular and cellular basis for this phenomenon, where large aggregates immediately manifest their deleterious effects. It may well be that the large assemblies of TDP-43 are more effective than small ones in recruiting TDP-43 from the nucleus (exacerbating both GOF and LOF), in recruiting and inactivating cytosolic proteins and RNAs, therefore acting as saboteurs, or in compromising the proteostasis network (PN).

The NSC-34 cells do not passively undergo the formation of the large and deleterious TDP-43 inclusions but degrade them using the two major clearance processes of the PN, i.e., UPS and ALP, as shown previously in other cellular systems (48–50). It is well known that UPS and ALP mainly degrade soluble and aggregated proteins, respectively, a finding also confirmed for TDP-43 in cultured cells (48). In our system, the clearance of the largest self-assemblies of TDP-43 diminishes upon UPS or ALP inhibition, indicating that both processes concur. This is mainly due to the presence, in addition to solid aggregates, of liquid-phase SGs of TDP-43 in our system, where liquid TDP-43 is in equilibrium with soluble monomeric TDP-43 amenable to UPS-mediated degradation, whereas it was mainly the TDP-43 solid microaggregates found to be cleared previously by ALP (48).

The question naturally arises as to why the inclusions continue to manifest their toxicity despite an apparently active PN. In fact, at 72 hours after transfection, the largest inclusions are cleared and the nuclear TDP-43 levels are restored, but cell viability is not fully recovered. To respond to this question, we need to consider
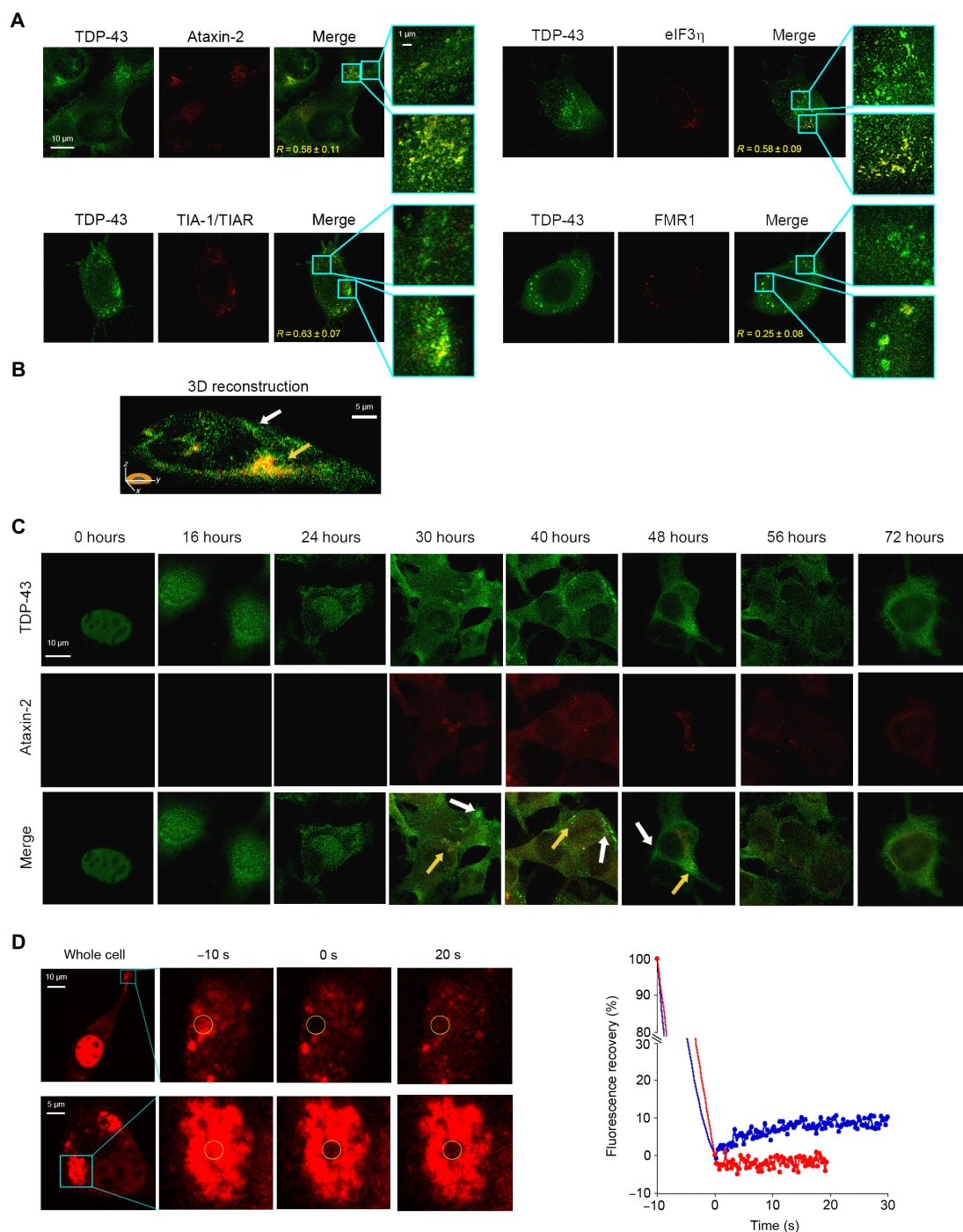
Fig. 6. TDP-43 is recruited to SGs, but the formation of TDP-43 inclusions is driven by different pathways. (**A**) Representative STED microscopy images of NSC-34 cells (*n* = 3) transfected with 20 μg of pCI-neo plasmid expressing human TDP-43 and observed at 40 hours after transfection. The green and red fluorescence indicate total TDP-43 (endogenous and exogenous) and the indicated SG markers, respectively. The top and bottom magnification boxes indicate areas with TDP-43 assemblies with a low and high degree of colocalization with SG markers, respectively. *R* values are indicated in merge images. (**B**) 3D reconstruction of the *z*-stack analysis (5-μm-thick slices) of the specimens shown in (A). A cell was virtually dissected on the *zy* plane to show the intracellular TDP-43 inclusions (green) with (yellow arrow) and without (blank arrow) colocalization with the SG marker ataxin-2 (red). (**C**) Representative confocal scanning microscopy images of NSC-34 cells (*n* = 3) transfected with 20 μg of pCI-neo plasmid expressing total TDP-43 (endogenous and exogenous) and analyzed after different lengths of time after transfection. The green and red fluorescence indicate TDP-43 and ataxin-2, respectively. Yellow and white arrows indicate TDP-43 inclusions with or without colocalization with ataxin-2, respectively. (**D**) Representative images of two TDP-43 inclusions in NSC-34 cells (*n* = 3) transfected with 25 μg of wtTDP43tdTOMATOHA plasmid expressing tdTOMATO-labeled human TDP-43 and observed at 40 hours after transfection. The yellow circled regions of interest (ROIs) were photobleached starting at time −10 s for 10 s, and FRAP was then monitored continuously for 20 to 30 s starting at time 0 s. FRAP was plotted over time (blue and red curves correspond to top and bottom panels, respectively). Fluorescence values were normalized to the average intensity of each ROI before photobleaching (−10 s).

that autophagy is a delicate system prone to malfunctioning. Although all events such as aggregate accumulation, TDP-43 nuclear loss and reactive oxygen species production have been shown to activate autophagy per se (*51–53*), and although all three events are observed to occur markedly in our neuronal model system starting at ca. 24 hours after transfection, nuclear loss of TDP-43 rather leads to failure of autophagy because nuclear TDP-43 stabilizes the autophagy-related 7 (ATG7) mRNA (*54*), promotes the correct splicing of ATG4B and B-cell lymphoma 2 (BCL2) pre-mRNAs (*55*, *56*), and activates the *dynactin 1* (*DCTN1*) gene essential for the autophagosome formation (*53*). A TDP-43–dependent impairment of the UPS is also observed (*57*, *58*). In this scenario, UPS and ALP are both activated and compromised, resulting in neurotoxicity. In support to this concept, the cells still contain many unresolved autophagy-related vesicles up to 72 hours, in agreement with observations that membrane-surrounded inclusions are abundant in spinal cord motor neurons of ALS cases (*59*) and indicating a dysfunctional stalled PN.

In conclusion, neuronal dysfunction in ALS and FTLD-U appears to be associated with changes of nuclear and cytoplasmic TDP-43 levels, wherein the largest cytoplasmic inclusions appear to play an important pathogenic role, as opposed to smaller assemblies. The possibility to identify and follow, in real time, the contributions of various aspects of TDP-43 localization and aggregation state to neuronal dysfunction allows us to rationalize many of the histopathological observations associated with TDP-43 proteinopathies.

MATERIALS AND METHODS
Experimental design
We aimed at developing an approach of quantitative biology to analyze simultaneously the time courses of TDP-43 nuclear levels, TDP-43 cytoplasmic levels, formation of cytoplasmic aggregates of various sizes, and neuronal dysfunction to elaborate a model of TDP-43 inclusion body formation and follow closely the link between neuronal dysfunction and specific aggregate types. We thus expressed human full-length TDP-43 in murine NSC-34 (as well as human SH-SY5Y cells to check applicability to another cell line) and exploited the high resolution of STED microscopy to monitor the formation of various classes of cytoplasmic TDP-43 aggregates as a function of time. Concomitantly, we monitored oxidative stress and mitochondrial impairment using the MitoSOX and MTT reduction assays, respectively, again, as a function of time. We then developed a mathematical model to describe the time courses of all these observables simultaneously in a quantitative manner and attribute a well-defined meaning to each of the observed phases, in terms of a mechanistic description of TDP-43 inclusion body formation and associated toxicity. We also evaluated whether the ALP and UPS systems were activated and responsible for specific phases of this process by using specific inhibitors, markers, and electron microscopy. Last, we monitored the involvement of SGs in the mechanism of TDP-43 inclusion body formation by evaluating the colocalization of TDP-43 inclusions with specific SGs markers and their liquid/solid phase using FRAP.

Cell culture
Murine NSC-34 is a hybrid motor neuron/neuroblastoma cell line that retains the ability to proliferate and express several motor neuron characteristics (*33*). NSC-34 cells were routinely maintained in Dulbecco's modified Eagle's medium (DMEM; D6429, Sigma-Aldrich), with 5% fetal bovine serum (FBS; F2442, Sigma-Aldrich), 1 mM glutamine (G7513, Sigma-Aldrich), 1.0% sodium pyruvate (S8636, Sigma-Aldrich), and antibiotics (P0781, Sigma-Aldrich; cell medium) in a 5% CO_2 humidified atmosphere at 37°C and grown until they reached 80% confluence, for a maximum of 20 passages (*8*, *49*). Authenticated human neuroblastoma SH-SY5Y cells were purchased from American Type Culture Collection (CRL-2266). They were tested negative for mycoplasma contaminations and were maintained cultured in DMEM (D6429, Sigma-Aldrich), F-12 Ham (N4888, Sigma-Aldrich) with 25 mM Hepes, and $NaHCO_3$ (1:1) supplemented with 10% FBS (F2442, Sigma-Aldrich), 1 mM glutamine (G7513, Sigma-Aldrich), and antibiotics (P0781, Sigma-Aldrich; cell medium) in a 5% CO_2 humidified atmosphere at 37°C and grown until 80% confluence for a maximum of 20 passages (*19*, *60*).

Transient transfection
Overexpression of TDP-43 was carried out using the pCI-neo plasmid expressing human TDP-43 (provided by E. Buratti, Italy) as previously reported (*8*). NSC-34 cells were plated in 12-well plates containing coverslips at a density of 75,000 cells per well. Twenty-four hours after plating, the cells were washed with phosphate-buffered saline (PBS) and transfected using Lipofectamine 3000 (L3000-008, Life Technologies), according to the manufacturer's instructions, with 0 to 20 μg of plasmid, 3.5 μl of Lipofectamine 3000 Reagent, 5 μl of transferrin (5 mg/liter), and 2.5 μl of P3000 reagent in DMEM for 3 hours in a 5% CO_2 humidified atmosphere at 37°C. After 3 hours (considered time, 0 hours of our time courses), the DMEM was replaced with fresh complete cell medium, the cells were incubated for different lengths of time (0 to 72 hours), and then STED images were acquired, as reported below. In a set of experiments, SH-SY5Y cells were plated in 12-well plates containing coverslips at a density of 45,000 cells per well, transfected after 24 hours with 20 μg of plasmid as reported above, and analyzed with STED microscopy in the following 0 to 72 hours. In another set of experiments, NSC-34 cells plated in 12-well plates were transfected with 20 μg of plasmid in the absence or presence of an RNA oligonucleotide (5′-GUGUGAAUGAAU-3′; BF400MO, Bio-Fab Research) at a concentration of 1 or 10 μM. The RNA was cotransfected with the pCI-neo plasmid or transfected 24 hours later (cotransfection and posttransfection, respectively).

STED microscopy
STED *xyz* images (*z* stacks acquired along the *x*/*y*/*z* axes) of NSC-34 cells were acquired in bidirectional mode using an SP8 STED 3X confocal microscope (Leica Microsystems), as previously reported (*60*). Total TDP-43 was monitored using 1:300 rabbit polyclonal anti–TDP-43 antibody (10782-2-AP, Proteintech) that recognized both the exogenous (human) and the endogenous (murine) protein, in PBS plus 1% FBS, for 60 min at 37°C, and then with 1:500 Alexa Fluor 568 (or Alexa Fluor 514)–conjugated secondary antibodies (A-11036 and A-31558, Invitrogen–Thermo Fisher Scientific), in PBS plus 1% FBS, for 60 min at 37°C. The analysis of phosphorylation of TDP-43 was assessed on NSC-34 cells plated in 12-well plates (density, 75,000 cells per well). After 0, 16, 40, and 56 hours of transient transfection with 20 μg of plasmid, phosphorylated TDP-43 was monitored using 1:500 rabbit anti–phospho–TDP-43 (pS409/410) antibodies (TIP-PTD-P01, Cosmo Bio Co. Ltd.) for 60 min at 37°C and then with 1:1000 Alexa Fluor 514–conjugated

secondary antibodies (A-11036, Invitrogen–Thermo Fisher Scientific) for 60 min at 37°C. Fluoromount-G (00-4958-02, Fisher Scientific) was used as mounting medium. Alexa Fluor 568 and Alexa Fluor 514 were excited with a 561- and 510-nm tuned white light laser (WLL), and emission was collected at 580 to 620 nm and 532 to 551 nm, respectively.

In the experiment for a 3D reconstruction of the whole cell, human TDP-43 was monitored using 1:300 mouse monoclonal anti-human TDP-43 antibody (60019-2-Ig, Proteintech) that recognized only the exogenous (human) protein, and the cell membrane was labeled with WGA tetramethylrhodamine (TMR) conjugate (W949, Life Technologies). TMR was excited with a 550-nm tuned WLL and emission collected at 564 to 599 nm.

Frame sequential acquisition was applied to avoid fluorescence overlap. A gating of 0.3 to 6 ns was applied to avoid collection of reflection and autofluorescence. Images were acquired with Leica HC PL APO CS2 100×/1.40 oil STED white objective, and gated pulsed STED was applied. Collected images were deconvolved with Huygens Professional software version 18.04 (Scientific Volume Imaging B.V.) and analyzed with Leica Application Suite X software (Leica Microsystems) to generate 3D reconstructions. Z-series stacks were obtained from 5-μm cell slices. Images were collected at 0.1-μm intervals.

Inclusion counting and size determination

In each STED image, the fluorescence background was subtracted, the nucleus area was excluded, and cytoplasmic inclusions were better defined in the images using the GNU Image Manipulation Program. The cytoplasmic area (A) of the analyzed cells was calculated as the fraction of pixels of the cytoplasm over the entire field and multiplying the obtained fraction by the area of the field in square micrometers. Cytoplasmatic inclusions were assigned to seven classes of aggregates with increasing diameter (0.025 to 0.15 μm, 0.15 to 0.25 μm, 0.25 to 0.50 μm, 0.50 to 0.75 μm, 0.75 to 1.00 μm, 1.00 to 1.50 μm, and >1.50 μm) and then counted using the ImageJ software. Class 7 (>1.50 μm) was excluded because of the presence of too few inclusions to provide a meaningful analysis. The number of each inclusion type (n) was divided by the cytoplasmic area (A, units of μm^2) of the neuron to obtain its density (D, units of n/μm^2). For each inclusion type, D was also multiplied by their mean area to provide the density of fluorescence associated with that given inclusion type [$F(t)/A$].

MTT reduction inhibition assay

Transient transfection was performed on NSC-34 cells plated in 96-well plates at a density of 15,000 cells per well with 4 μg of plasmid (corresponding to 20 μg of plasmid at 75,000 cells per well described in the "STED microscopy" section) for different lengths of time (0 to 72 hours), using 0.7 μl of Lipofectamine 3000 Reagent, 1 μl of transferrin (5 mg/liter), and 0.5 μl of P3000 reagent in DMEM for 3 hours in a 5% CO_2 humidified atmosphere at 37°C. The cells were then washed with PBS and incubated with an MTT solution (0.5 mg/ml) in RPMI medium at 37°C for 4 hours and then with cell lysis buffer [20% SDS and 50% N,N-dimethylformamide (pH 4.7)] for 1 hour. The absorbance values of blue formazan were determined at 595 nm by using an enzyme-linked immunosorbent assay plate reader (Bio-Rad). Cell viability was expressed as the percentage reduction of MTT in treated cells relative to cells treated with vehicle, to which a value of 100% was attributed. In another set of experiments, SH-SY5Y cells were plated in 96-well plates containing coverslips at a density of 10,000 cells per well and transfected with

4 μg of plasmid, and the MTT reduction test was performed following 0 to 72 hours, as reported above. In another set of experiments, NSC-34 cells plated in 96-well plates at a density of 15,000 cells per well were transfected with 4 μg of plasmid in the absence or presence of an RNA oligonucleotide (5′-GUGUGAAUGAAU-3′; BF400MO, Bio-Fab Research) at a concentration of 1 or 10 μM, and the MTT reduction assay was performed following 40 hours. The RNA was cotransfected with the pCI-neo plasmid or transfected 24 hours later (co-transf and post-transf, respectively). In all cases, the MTT assay was from Sigma-Aldrich (M5655).

Measurement of mitochondrial superoxide ions

Mitochondrial superoxide ion production was detected with a static time point measurement in living NSC-34 cells by using the Mito-SOX Red Mitochondrial Superoxide Indicator (TM36008, Thermo Fisher Scientific). Cells were plated in 12-well plates containing coverslips and transiently transfected as described above (see the "Transient transfection" section). At different lengths of time after transfection (0 to 72 hours), cells were treated with the MitoSOX probe for 10 min. Fluorescence emission was detected after excitation at 550 nm by the TCS SP8 scanning confocal microscopy system (Leica Microsystems) equipped with an argon laser source. A series of 1.0-μm-thick optical sections (1024 × 1024 pixels) was taken through the cell depth for each sample using a Leica Plan Apo 63× oil immersion objective and projected as a single composite image by superimposition. The confocal microscope was set at optimal acquisition conditions, e.g., pinhole diameters, detector gain, and laser powers. Settings were maintained constant for each analysis.

Theoretical analysis of MTT reduction and MitoSOX data

Each MTT reduction and mitochondrial superoxide production value at a given time point t was analyzed with a least squares linear regression fitting procedure using

$$\text{MTT-R}(t) = 100 - [c\Delta C(t) + n\Delta N(t)] \quad (1)$$

$$\text{MitoSOX}(t) = 100 + [c\Delta C(t) + n\Delta N(t)] \quad (2)$$

where MTT-R(t) and MitoSOX(t) are the percent values of MTT reduction and mitochondrial superoxide production, respectively, at time t relative to time 0 hours, $\Delta C(t)$ and $\Delta N(t)$ are the changes of cytoplasmic and nuclear TDP-43 levels at the same time t relative to time 0 hours, respectively, and c and n are their corresponding proportionality constants, respectively. All data points of MTT-R(t) were analyzed simultaneously with Eq. 1, using the corresponding and experimentally determined $\Delta C(t)$ and $\Delta N(t)$ values, and with c and n values free to float in the fitting procedure but kept constant all time points. Correspondingly, all data points of MitoSOX(t) were analyzed simultaneously with Eq. 2. Note that the c and n values determined from the two analyses are different because of differences in MTT-R(t) and Mitosox(t) values, which decrease and increase with time to different degrees. The best-fitted values of c and n from the MTT-R(t) analysis were then used to determine the relative contributions of nuclear depletion and cytoplasmic accumulation of TDP-43, respectively, in determining the change in MTT reduction, using

$$c(\%) = c/(c+n) \qquad n(\%) = n\ (c+n) \quad (3)$$

The analysis was repeated using the best-fitted values of c and n from the MitoSOX(t) analysis, again, using Eq. 3. The whole analysis was then repeated from the beginning by considering only the $c\Delta C(t)$ and $n\Delta N(t)$ contributions in Eqs. 1 and 2. This was achieved constraining n to 0 in Eq. 1 or 2 and c to 0 in Eq. 1 or 2, respectively.

Theoretical analysis of TDP-43 cytoplasmic inclusion data

The time courses of the fluorescence associated with the six classes of aggregates were analyzed with a kinetic sigmoid function of logistic type consisting of three exponential phases and their lag times. For small aggregates (diameter, 0.025 to 0.15 μm), it was

$$F(t)/A = \frac{A_{1,2}}{(\exp(-k_1(t - \mathrm{lag}_{1,2})) + \exp(k_2(t - \mathrm{lag}_{1,2})))} + \frac{A_3}{(1 + \exp(-k_3(t - \mathrm{lag}_3)))} \qquad (4)$$

where $F(t)/A$ is the total fluorescence density at time t associated with inclusions of that size; $A_{1,2}$ and A_3 are the amplitudes of the first (and second) and third phases, respectively; k_1, k_2, and k_3 are the rate constants of the three phases, respectively; and $\mathrm{lag}_{1,2}$ and lag_3 are the lag times of the first (and second) and third phases, respectively.

For all other classes of TDP-43 inclusions (diameters from 0.15 to 0.25 μm to 1.0 to 1.5 μm), it was

$$F(t)/A = \frac{A_{1,2}}{1 + \exp(-k_2(t - \mathrm{lag}_{1,2}))} + \frac{A_3}{(1 + \exp(-k_3(t - \mathrm{lag}_3)))} \qquad (5)$$

where the parameters have the same meaning as in Eq. 4. The time course of a seventh class (diameter, 1.5 to 2.0 μm) was not analyzed given the limited number of inclusions. Since the first phase only involves the formation of the first class of the smallest inclusions, it was omitted in Eq. 5. All six time courses were fitted simultaneously. However, given the multiplicity of parameters to be fitted, the rate constants k_1, k_2, and k_3 and the lag times $\mathrm{lag}_{1,2}$ and lag_3 were initially fixed to reasonable arbitrary values, and the remaining parameters describing phase amplitudes ($A_{1,2}$ and A_3) were left free to float in six independent fitting procedures (one per time course). Once six pairs of $A_{1,2}/A_3$ values were identified (one pair per time course), the remaining k_1, k_2, k_3, $\mathrm{lag}_{1,2}$, and lag_3 were allowed to float simultaneously in the six time courses in one single fitting procedure. In particular, the k_1, k_2, and k_3 values were left to float freely but simultaneously in the six time courses (so that a single set of k_1, k_2, and k_3 values could be determined in all six time courses). The $\mathrm{lag}_{1,2}$ and lag_3 times were left to float independently in the six time courses, but with constant delays in the various time courses, so that $\mathrm{lag}_{1,2}$ and lag_3 of the $i + 1$ time course were $\mathrm{lag}_{1,2} + d_{1,2}$ and $\mathrm{lag}_3 + d_3$ of the i time course (where $d_{1,2}$ and d_3 were constant). The $d_{1,2}$ and d_3 values account for the delayed appearances and anticipated decay of the second and third phases of a given inclusion type relative to the smaller class, respectively.

Inhibition of ALP and UPS

Cells were plated in 12-well plates containing coverslips, transfected as indicated above (see the "Transient transfection" section), and treated at 38 hours after transfection with 5 μM MG132 (M7449, Sigma-Aldrich) or 10 mM 3-MA (5142-23-4, Sigma-Aldrich), and STED images were acquired at 40, 56, and 72 hours after cell transfection, as indicated above (see the "STED microscopy" section).

Analysis of the colocalization of TDP-43 with lysosomes and early endosomes

NSC-34 cells were plated in 12-well plates and transfected as indicated above (see the "Transient transfection" section). Twenty-four hours after transfection, CellLight lysosomes-RFP (C10597, Invitrogen–Thermo Fisher Scientific) or early endosomes-RFP constructs (C10587, Invitrogen–Thermo Fisher Scientific) were added to the cells. Following an overnight incubation (40 hours after the TDP-43 transfection), cells were washed with PBS, fixed in 2% (w/v) buffered paraformaldehyde for 10 min at 20°C, and permeabilized with a 0.5% (v/v) Triton X-100 solution for 5 min. TDP-43 was monitored using mouse monoclonal anti-human TDP-43 antibody (60019-2-Ig, Proteintech) for 60 min at 37°C and then with 1:500 Alexa Fluor 514–conjugated secondary antibodies (A-31555, Invitrogen–Thermo Fisher Scientific) for 60 min at 37°C. Then, a STED microscopy analysis was performed as described above.

Transmission electron microscopy

NSC-34 cells transfected with vehicle or TDP-43 were washed out in 0.1 M cacodylate buffer (C0250, Sigma-Aldrich) and fixed in 0.1 M cacodylate buffer containing 2.5% glutaraldehyde (16365, Electron Microscopy Sciences) for 1 hour at room temperature. The cells were postfixed in 1% osmium tetroxide (19100, Electron Microscopy Sciences) for 1 hour, 1% tannic acid (W304204, Sigma-Aldrich) for 30 min, and 1% aqueous uranyl acetate (77870.01, SERVA, Heidelberg, DE) for 1 hour. Subsequently, samples were dehydrated through a graded ethanol series and flat-embedded in resin (14120, Electron Microscopy Sciences) for 24 hours at 60°C. Ultrathin sections (50 nm) were cut parallel to the substrate and counterstained with 5% uranyl acetate in 50% ethanol. Electron micrographs were acquired with a Hitachi 7800 120-kV TEM (Hitachi) equipped with MegaView G3 digital camera and RADIUS software (EMSIS) using the Multiple Image Alignment montage tool.

Analysis of the colocalization of TDP-43 within SGs

NSC-34 cells were plated in 12-well plates and transfected as indicated above (see the "Transient transfection" section). Forty hours later, the cells were washed with PBS, fixed in 2% (w/v) buffered paraformaldehyde for 10 min at 20°C, and permeabilized with a 0.5% (v/v) Triton X-100 solution for 5 min. Immunocytochemistry was carried out using 1:300 rabbit polyclonal anti–TDP-43 antibody (10782-2-AP, Proteintech) and mouse monoclonal anti–Ataxin-2 antibody (sc-515602, Santa Cruz Biotechnology), anti-TIA-1/TIAR antibody (sc-48371, Santa Cruz Biotechnology), anti-eIF3η antibody (sc-137214, Santa Cruz Biotechnology), or anti-FMR1 (sc-101048, Santa Cruz Biotechnology) for 60 min at 37°C and then with 1:500 Alexa Fluor 514–conjugated secondary antibodies (A-31555, Invitrogen–Thermo Fisher Scientific) and Alexa Fluor 568–conjugated secondary antibodies (A-11004, Invitrogen–Thermo Fisher Scientific) for 60 min at 37°C. The colocalization with Ataxin-2 was also monitored at different lengths of time after transfection (0 to 72 hours). STED images were then acquired as described above. The colocalization of TDP-43 assemblies and SGs was estimated in regions of interest (ROIs), and the linear correlation coefficient (R) value was calculated via the use of ImageJ (National Institutes of Health, Bethesda, MD, USA) and JACoP plugin.

Fluorescence recovery after photobleaching

NSC-34 cells were plated in eight-well plates (density, 22,500 cells per well) and transfected with 25 μg of wtTDP43tdTOMATOHA plasmid (28205, Addgene) using 1.1 μl of Lipofectamine 3000 Reagent, 1.5 μl of transferrin (5 mg/liter), and 0.75 μl of P3000 reagent in DMEM for 3 hours in a 5% CO_2 humidified atmosphere at 37°C. After 3 hours, the DMEM was replaced with fresh complete cell medium, and the FRAP experiment was performed after 40 hours using the LAS AF FRAP Application Wizard on the Leica TCS SP8 3× microscope. Images were acquired using the Leica HC PL APO CS2 100×/1.40 oil white objective and the 554-nm laser, at a scan speed of 700 Hz. A prebleach image was acquired with a laser power of 20%. Photobleaching was then performed for 10 s in ROIs containing TDP-43 inclusions, at 60 to 80% laser intensity. Fluorescence recovery was then monitored for 20 to 30 s by setting the laser power back to 20%.

Statistical analysis

Data were expressed as means ± SEM. Comparisons between different groups were performed by using analysis of variance (ANOVA) followed by Bonferroni's post comparison test by using GraphPad Prism 7.0 software. A value of $P < 0.05$ was considered to be statistically significant. The agreement between theoretical and experimental data was evaluated determining the R and corresponding P values in plots of theoretical versus experimental values. A value of $P < 0.05$ was considered to be statistically significant.

SUPPLEMENTARY MATERIALS
Supplementary material for this article is available at https://science.org/doi/10.1126/sciadv.abm6376

View/request a protocol for this paper from *Bio-protocol*.

REFERENCES AND NOTES

1. T. Arai, M. Hasegawa, H. Akiyama, K. Ikeda, T. Nonaka, H. Mori, D. Mann, K. Tsuchiya, M. Yoshida, Y. Hashizume, T. Oda, TDP-43 is a component of ubiquitin-positive tau-negative inclusions in frontotemporal lobar degeneration and amyotrophic lateral sclerosis. *Biochem. Biophys. Res. Commun.* **351**, 602–611 (2006).
2. M. Neumann, D. M. Sampathu, L. K. Kwong, A. C. Truax, M. C. Micsenyi, T. T. Chou, J. Bruce, T. Schuck, M. Grossman, C. M. Clark, L. F. McCluskey, B. L. Miller, E. Masliah, I. R. Mackenzie, H. Feldman, W. Feiden, H. A. Kretzschmar, J. Q. Trojanowski, V. M. Y. Lee, Ubiquitinated TDP-43 in frontotemporal lobar degeneration and amyotrophic lateral sclerosis. *Science* **314**, 130–133 (2006).
3. I. R. Mackenzie, E. H. Bigio, P. G. Ince, F. Geser, M. Neumann, N. J. Cairns, L. K. Kwong, M. S. Forman, J. Ravits, H. Stewart, A. Eisen, L. McClusky, H. A. Kretzschmar, C. M. Monoranu, J. R. Highley, J. Kirby, T. Siddique, P. J. Shaw, V. M. Lee, J. Q. Trojanowski, Pathological TDP-43 distinguishes sporadic amyotrophic lateral sclerosis from amyotrophic lateral sclerosis with SOD1 mutations. *Ann. Neurol.* **61**, 427–434 (2007).
4. J. Brettschneider, K. Del Tredici, J. B. Toledo, J. L. Robinson, D. J. Irwin, M. Grossman, E. Suh, V. M. Van Deerlin, E. M. Wood, Y. Baek, L. Kwong, E. B. Lee, L. Elman, L. McCluskey, L. Fang, S. Feldengut, A. C. Ludolph, V. M. Lee, H. Braak, J. Q. Trojanowski, Stages of pTDP-43 pathology in amyotrophic lateral sclerosis. *Ann. Neurol.* **74**, 20–38 (2013).
5. M. Hasegawa, T. Arai, T. Nonaka, F. Kametani, M. Yoshida, Y. Hashizume, T. G. Beach, E. Buratti, F. Baralle, M. Morita, I. Nakano, T. Oda, K. Tsuchiya, H. Akiyama, Phosphorylated TDP-43 in frontotemporal lobar degeneration and amyotrophic lateral sclerosis. *Ann. Neurol.* **64**, 60–70 (2008).
6. L. M. Igaz, L. K. Kwong, Y. Xu, A. C. Truax, K. Uryu, M. Neumann, C. M. Clark, L. B. Elman, B. L. Miller, M. Grossman, L. F. McCluskey, J. Q. Trojanowski, V. M. Lee, Enrichment of C-terminal fragments in TAR DNA-binding protein-43 cytoplasmic inclusions in brain but not in spinal cord of frontotemporal lobar degeneration and amyotrophic lateral sclerosis. *Am. J. Pathol.* **173**, 182–194 (2008).
7. G. Halliday, E. H. Bigio, N. J. Cairns, M. Neumann, I. R. Mackenzie, D. M. Mann, Mechanisms of disease in frontotemporal lobar degeneration: Gain of function versus loss of function effects. *Acta Neuropathol.* **124**, 373–382 (2012).
8. R. Cascella, C. Capitini, G. Fani, C. M. Dobson, C. Cecchi, F. Chiti, Quantification of the relative contributions of loss-of-function and gain-of-function mechanisms in TAR DNA-binding protein 43 (TDP-43) proteinopathies. *J. Biol. Chem.* **291**, 19437–19448 (2016).
9. C. Amador-Ortiz, W. L. Lin, Z. Ahmed, D. Personett, P. Davies, R. Duara, N. R. Graff-Radford, M. L. Hutton, D. W. Dickson, TDP-43 immunoreactivity in hippocampal sclerosis and Alzheimer's disease. *Ann. Neurol.* **61**, 435–445 (2007).
10. H. Nakashima-Yasuda, K. Uryu, J. Robinson, S. X. Xie, H. Hurtig, J. E. Duda, S. E. Arnold, A. Siderowf, M. Grossman, J. B. Leverenz, R. Woltjer, O. L. Lopez, R. Hamilton, D. W. Tsuang, D. Galasko, E. Masliah, J. Kaye, C. M. Clark, T. J. Montine, V. M. Y. Lee, J. Q. Trojanowski, Co-morbidity of TDP-43 proteinopathy in Lewy body related diseases. *Acta Neuropathol.* **114**, 221–229 (2007).
11. C. Schwab, T. Arai, M. Hasegawa, S. Yu, P. L. McGeer, Colocalization of transactivation-responsive DNA-binding protein 43 and huntingtin in inclusions of Huntington disease. *J. Neuropathol. Exp. Neurol.* **67**, 1159–1165 (2008).
12. R. H. Baloh, TDP-43: The relationship between protein aggregation and neurodegeneration in amyotrophic lateral sclerosis and frontotemporal lobar degeneration. *FEBS J.* **278**, 3539–3549 (2011).
13. M. T. Giordana, M. Piccinini, S. Grifoni, G. De Marco, M. Vercellino, M. Magistrello, A. Pellerino, B. Buccinnà, E. Lupino, M. T. Rinaudo, TDP-43 redistribution is an early event in sporadic amyotrophic lateral sclerosis. *Brain Pathol.* **20**, 351–360 (2010).
14. H. Braak, A. Ludolph, D. R. Thal, K. Del Tredici, Amyotrophic lateral sclerosis: Dash-like accumulation of phosphorylated TDP-43 in somatodendritic and axonal compartments of somatomotor neurons of the lower brainstem and spinal cord. *Acta Neuropathol.* **120**, 67–74 (2010).
15. W. L. Lin, D. W. Dickson, Ultrastructural localization of TDP-43 in filamentous neuronal inclusions in various neurodegenerative diseases. *Acta Neuropathol.* **116**, 205–213 (2008).
16. J. R. Thorpe, H. Tang, J. Atherton, N. J. Cairns, Fine structural analysis of the neuronal inclusions of frontotemporal lobar degeneration with TDP-43 proteinopathy. *J. Neural Transm. (Vienna)* **115**, 1661–1671 (2008).
17. A. Kerman, N. H. Liu, S. Croul, J. Bilbao, E. Rogaeva, L. Zinman, J. Robertson, A. Chakrabartty, Amyotrophic lateral sclerosis is a non-amyloid disease in which extensive misfolding of SOD1 is unique to the familial form. *Acta Neuropathol.* **119**, 335–344 (2010).
18. N. J. Cairns, M. Neumann, E. H. Bigio, I. E. Holm, D. Troost, K. J. Hatanpaa, C. Foong, C. L. White III, J. A. Schneider, H. A. Kretzschmar, D. Carter, L. Taylor-Reinwald, K. Paulsmeyer, J. Strider, M. Gitcho, A. M. Goate, J. C. Morris, M. Mishra, L. K. Kwong, A. Stieber, Y. Xu, M. S. Forman, J. Q. Trojanowski, V. M. Lee, I. R. Mackenzie, TDP-43 in familial and sporadic frontotemporal lobar degeneration with ubiquitin inclusions. *Am. J. Pathol.* **171**, 227–240 (2007).
19. C. Capitini, S. Conti, M. Perni, F. Guidi, R. Cascella, A. De Poli, A. Penco, A. Relini, C. Cecchi, F. Chiti, TDP-43 inclusion bodies formed in bacteria are structurally amorphous, non-amyloid and inherently toxic to neuroblastoma cells. *PLOS ONE* **9**, e86720 (2014).
20. Y. Sun, A. Medina Cruz, K. C. Hadley, N. J. Galant, R. Law, R. M. Vernon, V. K. Morris, J. Robertson, A. Chakrabartty, Physiologically important electrolytes as regulators of TDP-43 aggregation and droplet-phase behavior. *Biochemistry* **58**, 590–607 (2019).
21. D. Arseni, M. Hasegawa, A. G. Murzin, F. Kametani, M. Arai, M. Yoshida, B. Ryskeldi-Falcon, Structure of pathological TDP-43 filaments from ALS with FTLD. *Nature* **601**, 139–143 (2022).
22. L. McGurk, E. Gomes, L. Guo, J. Mojsilovic-Petrovic, V. Tran, R. G. Kalb, J. Shorter, N. M. Bonini, Poly(ADP-ribose) prevents pathological phase separation of TDP-43 by promoting liquid demixing and stress granule localization. *Mol. Cell* **71**, 703–717.e9 (2018).
23. C. Capitini, G. Fani, A. Vivoli Vega, A. Penco, C. Canale, L. D. Cabrita, M. Calamai, J. Christodoulou, A. Relini, F. Chiti, Full-length TDP-43 and its C-terminal domain form filaments in vitro having non-amyloid properties. *Amyloid* **28**, 56–65 (2021).
24. F. Gasset-Rosa, S. Lu, H. Yu, C. Chen, Z. Melamed, L. Guo, J. Shorter, S. Da Cruz, D. W. Cleveland, Cytoplasmic TDP-43 de-mixing independent of stress granules drives inhibition of nuclear import, loss of nuclear TDP-43, and cell death. *Neuron* **102**, 339–357.e7 (2019).
25. Y. Chen, T. J. Cohen, Aggregation of the nucleic acid-binding protein TDP-43 occurs via distinct routes that are coordinated with stress granule formation. *J. Biol. Chem.* **294**, 3696–3706 (2019).
26. F. Hans, H. Glasebach, P. J. Kahle, Multiple distinct pathways lead to hyperubiquitylated insoluble TDP-43 protein independent of its translocation into stress granules. *J. Biol. Chem.* **295**, 673–689 (2020).
27. L. M. Igaz, L. K. Kwong, A. Chen-Plotkin, M. J. Winton, T. L. Unger, Y. Xu, M. Neumann, J. Q. Trojanowski, V. M. Lee, Expression of TDP-43 C-terminal fragments in vitro recapitulates pathological features of TDP-43 proteinopathies. *J. Biol. Chem.* **284**, 8516–8524 (2009).
28. Y. J. Zhang, Y. F. Xu, C. Cook, T. F. Gendron, P. Roettges, C. D. Link, W. L. Lin, J. Tong, M. Castanedes-Casey, P. Ash, J. Gass, V. Rangachari, E. Buratti, F. Baralle, T. E. Golde, D. W. Dickson, L. Petrucelli, Aberrant cleavage of TDP-43 enhances aggregation and cellular toxicity. *Proc. Natl. Acad. Sci. U.S.A.* **106**, 7607–7612 (2009).

29. T. Nonaka, F. Kametani, T. Arai, H. Akiyama, M. Hasegawa, Truncation and pathogenic mutations facilitate the formation of intracellular aggregates of TDP-43. *Hum. Mol. Genet.* **18**, 3353–3364 (2009).

30. M. J. Winton, L. M. Igaz, M. M. Wong, L. K. Kwong, J. Q. Trojanowski, V. M. Y. Lee, Disturbance of nuclear and cytoplasmic TAR DNA-binding protein (TDP-43) induces disease-like redistribution, sequestration, and aggregate formation. *J. Biol. Chem.* **283**, 13302–13309 (2008).

31. Y. M. Ayala, P. Zago, A. D'Ambrogio, Y.-F. Xu, L. Petrucelli, E. Buratti, F. E. Baralle, Structural determinants of the cellular localization and shuttling of TDP-43. *J. Cell Sci.* **121**(Pt. 22), 3778–3785 (2008).

32. A. L. Nishimura, V. Zupunski, C. Troakes, C. Kathe, P. Fratta, M. Howell, J. M. Gallo, T. Hortobágyi, C. E. Shaw, B. Rogelj, Nuclear import impairment causes cytoplasmic trans-activation response DNA-binding protein accumulation and is associated with frontotemporal lobar degeneration. *Brain* **133**, 1763–1771 (2010).

33. N. R. Cashman, H. D. Durham, J. K. Blusztajn, K. Oda, T. Tabira, I. T. Shaw, S. Dahrouge, J. P. Antel, Neuroblastoma x spinal cord (NSC) hybrid cell lines resemble developing motor neurons. *Dev. Dyn.* **194**, 209–221 (1992).

34. J. C. Rengifo-Gonzalez, K. El Hage, M. J. Clément, E. Steiner, V. Joshi, P. Craveur, D. Durand, D. Pastré, A. Bouhss, The cooperative binding of TDP-43 to GU-rich RNA repeats antagonizes TDP-43 aggregation. *eLife* **10**, e67605 (2021).

35. A. Raimondi, A. Mangolini, M. Rizzardini, S. Tartari, S. Massari, C. Bendotti, M. Francolini, N. Borgese, L. Cantoni, G. Pietrini, Cell culture models to investigate the selective vulnerability of motoneuronal mitochondria to familial ALS-linked G93ASOD1. *Eur. J. Neurosci.* **24**, 387–399 (2006).

36. P. Rusmini, K. Cortese, V. Crippa, R. Cristofani, M. E. Cicardi, V. Ferrari, G. Vezzoli, B. Tedesco, M. Meroni, E. Messi, M. Piccolella, M. Galbiati, M. Garrè, E. Morelli, T. Vaccari, A. Poletti, Trehalose induces autophagy via lysosomal-mediated TFEB activation in models of motoneuron degeneration. *Autophagy* **15**, 631–651 (2019).

37. M. Ralser, M. Albrecht, U. Nonhoff, T. Lengauer, H. Lehrach, S. Krobitsch, An integrative approach to gain insights into the cellular function of human ataxin-2. *J. Mol. Biol.* **346**, 203–214 (2005).

38. N. L. Kedersha, M. Gupta, W. Li, I. Miller, P. Anderson, RNA-binding proteins TIA-1 and TIAR link the phosphorylation of eIF-2 alpha to the assembly of mammalian stress granules. *J. Cell Biol.* **147**, 1431–1442 (1999).

39. N. Kedersha, S. Chen, N. Gilks, W. Li, I. J. Miller, J. Stahl, P. Anderson, Evidence that ternary complex (eIF2-GTP-tRNA(i)(Met))-deficient preinitiation complexes are core constituents of mammalian stress granules. *Mol. Biol. Cell* **13**, 195–210 (2002).

40. S. H. Kim, W. K. Dong, I. J. Weiler, W. T. Greenough, Fragile X mental retardation protein shifts between polyribosomes and stress granules after neuronal injury by arsenite stress or in vivo hippocampal electrode insertion. *J. Neurosci.* **26**, 2413–2318 (2006).

41. P. P. Gopal, J. J. Nirschl, E. Klinman, E. L. Holzbaur, Amyotrophic lateral sclerosis-linked mutations increase the viscosity of liquid-like TDP-43 RNP granules in neurons. *Proc. Natl. Acad. Sci. U.S.A.* **114**, E2466–E2475 (2017).

42. H. L. Roberts, D. R. Brown, Seeking a mechanism for the toxicity of oligomeric α-synuclein. *Biomolecules* **5**, 282–305 (2015).

43. I. Benilova, E. Karran, B. De Strooper, The toxic Aβ oligomer and Alzheimer's disease: An emperor in need of clothes. *Nat. Neurosci.* **15**, 349–357 (2012).

44. M. J. Guerrero-Muñoz, J. Gerson, D. L. Castillo-Carranza, Tau oligomers: The toxic player at synapses in Alzheimer's disease. *Front. Cell. Neurosci.* **9**, 464 (2015).

45. F. Chiti, C. M. Dobson, Protein misfolding, amyloid formation, and human disease: A summary of progress over the last decade. *Annu. Rev. Biochem.* **86**, 27–68 (2017).

46. H. Sumi, S. Kato, Y. Mochimaru, H. Fujimura, M. Etoh, S. Sakoda, Nuclear TAR DNA binding protein 43 expression in spinal cord neurons correlates with the clinical course in amyotrophic lateral sclerosis. *J. Neuropathol. Exp. Neurol.* **68**, 37–47 (2009).

47. J. Brettschneider, K. Arai, K. Del Tredici, J. B. Toledo, J. L. Robinson, E. B. Lee, S. Kuwabara, K. Shibuya, D. J. Irwin, L. Fang, V. M. Van Deerlin, L. Elman, L. McCluskey, A. C. Ludolph, V. M. Lee, H. Braak, J. Q. Trojanowski, TDP-43 pathology and neuronal loss in amyotrophic lateral sclerosis spinal cord. *Acta Neuropathol.* **128**, 423–437 (2014).

48. E. L. Scotter, C. Vance, A. L. Nishimura, Y. B. Lee, H. J. Chen, H. Urwin, V. Sardone, J. C. Mitchell, B. Rogelj, D. C. Rubinsztein, C. E. Shaw, Differential roles of the ubiquitin proteasome system and autophagy in the clearance of soluble and aggregated TDP-43 species. *J. Cell Sci.* **127**(Pt. 6), 1263–1278 (2014).

49. R. Cascella, G. Fani, C. Capitini, P. Rusmini, A. Poletti, C. Cecchi, F. Chiti, Quantitative assessment of the degradation of aggregated TDP-43 mediated by the ubiquitin proteasome system and macroautophagy. *FASEB J.* **31**, 5609–5624 (2017).

50. M. Urushitani, T. Sato, H. Bamba, Y. Hisa, I. Tooyama, Synergistic effect between proteasome and autophagosome in the clearance of polyubiquitinated TDP-43. *J. Neurosci. Res.* **88**, 784–797 (2010).

51. J. Labbadia, R. I. Morimoto, The biology of proteostasis in aging and disease. *Annu. Rev. Biochem.* **84**, 435–464 (2015).

52. R. Scherz-Shouval, E. Shvets, E. Fass, H. Shorer, L. Gil, Z. Elazar, Reactive oxygen species are essential for autophagy and specifically regulate the activity of Atg4. *EMBO J.* **26**, 1749–1760 (2007).

53. Q. Xia, H. Wang, Z. Hao, C. Fu, Q. Hu, F. Gao, H. Ren, D. Chen, J. Han, Z. Ying, G. Wang, TDP-43 loss of function increases TFEB activity and blocks autophagosome-lysosome fusion. *EMBO J.* **35**, 121–142 (2016).

54. J. K. Bose, C.-C. Huang, C. J. K. Shen, Regulation of autophagy by neuropathological protein TDP-43. *J. Biol. Chem.* **286**, 44441–44448 (2011).

55. J. P. Ling, O. Pletnikova, J. C. Troncoso, P. C. Wong, TDP-43 repression of nonconserved cryptic exons is compromised in ALS-FTD. *Science* **349**, 650–655 (2015).

56. S.-L. Huang, L.-S. Wu, M. Lee, C.-W. Chang, W.-C. Cheng, Y.-S. Fang, Y.-R. Chen, P.-L. Cheng, C. J. Shen, A robust TDP-43 knock-in mouse model of ALS. *Acta Neuropathol. Commun.* **8**, 3 (2020).

57. F. B. Lee, V. M. Lee, J. Q. Trojanowski, Gains or losses: Molecular mechanisms of TDP43-mediated neurodegeneration. *Nat. Rev. Neurosci.* **13**, 38–50 (2011).

58. H. Tagashira, Y. Shinoda, N. Shioda, K. Fukunaga, Methyl pyruvate rescues mitochondrial damage caused by SIGMAR1 mutation related to amyotrophic lateral sclerosis. *Biochim. Biophys. Acta* **1840**, 3320–3334 (2014).

59. S. Sasaki, Autophagy in spinal cord motor neurons in sporadic amyotrophic lateral sclerosis. *J. Neuropathol. Exp. Neurol.* **70**, 349–359 (2011).

60. R. Cascella, S. W. Chen, A. Bigi, J. D. Camino, C. K. Xu, C. M. Dobson, F. Chiti, N. Cremades, C. Cecchi, The release of toxic oligomers from α-synuclein fibrils induces dysfunction in neuronal cells. *Nat. Commun.* **12**, 1814 (2021).

Use of this article is subject to the Terms of service